J. Fluid Mech. (2024), *vol*. 984, A52, doi:10.1017/jfm.2024.196

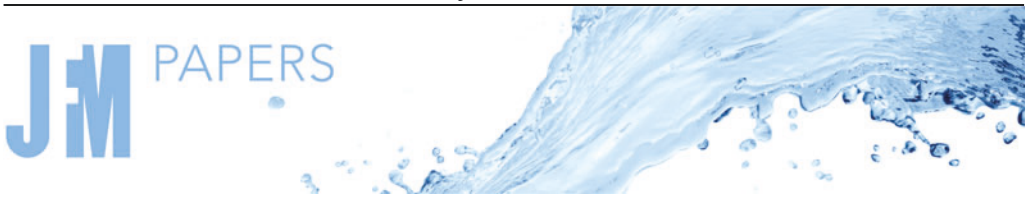

Elastic particle model for coil-stretch transition of dilute polymers in an elongational flow

Tong Gao[1,2]†

[1]Department of Mechanical Engineering, Michigan State University, East Lansing, MI 48864, USA

[2]Department of Computational Mathematics, Science and Engineering, Michigan State University, East Lansing, MI 48864, USA

(Received 9 July 2023; revised 1 January 2024; accepted 23 February 2024)

The phenomenon of the 'coil-stretch' (C-S) transition, wherein a long-chain polymer initially in a coiled state undergoes a sudden configuration change to become fully stretched under steady elongational flows, has been widely recognized. This transition can display intricate hysteresis behaviours under specific critical conditions, giving rise to unique rheological characteristics in dilute polymer solutions. Historically, microscopic stochastic models and Brownian dynamics simulations have shed light on the underlying mechanisms of the transition by uncovering bistable configurations of polymer chains. Following the initial work by Cerf (*J. Chem. Phys.*, vol. 20, 1952, pp. 395–402), we introduce a continuum model in this study to investigate the C-S transition in a constant uniaxial elongational flow. Our approach involves approximating the unfolding process of the polymer chain as an axisymmetric deformation of an elastic particle. We make the assumption that the particle possesses uniform material properties, which can be represented by a nonlinear, strain-hardening constitutive equation to replicate the finite extensibility of the polymer chain. Subsequently, we analytically solve for the steady-state deformation using a polarization method. By employing this reduced model, we effectively capture the C-S transition and establish its specific correlations with material and geometric properties. The hysteresis phenomena can be comprehended through a force-balance analysis, which involves comparing the externally applied viscous forces with the intrinsic elastic responsive forces. We demonstrate that our model, while simple, unveils rich elastohydrodynamics of the C-S transition.

Key words: multiphase flow, suspensions

† Email address for correspondence: gaotong@egr.msu.edu

1. Introduction

Understanding the interactions of polymer molecules and hydrodynamic flows are among the most fundamental topics in the interdisciplinary research areas of fluid mechanics, chemical engineering and polymer physics (Lumley 1969; Bird 1987). When subjected to various flow conditions, polymer molecule may exhibit rich behaviours of morphing chain configurations as revealed by single molecule visualization techniques (Perkins, Smith & Chu 1997; Smith, Babcock & Chu 1999), leading to intriguing bulk rheological and physical properties (Fuller & Leal 1980; Menasveta & Hoagland 1991; Hunkeler, Nguyen & Kausch 1996; Lee *et al.* 2007). Of particular interest is the study of the coil-stretch (C-S) transition of long-chain macromolecules, such as DNAs, in flows of dilute solutions. When the background flow has a non-zero velocity gradient (e.g. shear and elongational flows), at certain critical conditions, the coiled polymers can abruptly unwind to become elongated or fully stretched shapes due to the imposed fluid viscous force, termed as the C-S transition (Smith & Chu 1998). More interestingly, when measuring the polymer's end-to-end distance as a function of the extension rate, the transition typically features hysteresis behaviours, suggesting a bistable system with more than one equilibrium state.

In the early 1970s, DeGennes (1974) introduced the initial kinetic model of an elastic dumbbell to predict the hysteresis behaviours observed in elongational flows during the C-S transition. He attributed these phenomena to the shape-dependent viscous force acting on the polymer chain. As the DNA unfolds, the initially hidden monomers become more exposed to hydrodynamic flows. By not explicitly considering fluid–polymer interactions, de Gennes demonstrated that the hysteresis behaviours can be effectively described by a double-well potential, which combines the effects of the background elongational flow and the elastic forces in the dumbbell spring. The same mechanism was pointed out independently by Hinch (1974, 1977) and was supported by several other authors (Tanner 1975; Fuller & Leal 1981). Instead of using phenomenological double-well potentials, they resolved the hysteresis using similar elastic dumbbell models that incorporated length-dependent hydrodynamic friction forces. Apart from the hydrodynamic effects, all these models emphasized the importance of employing nonlinear elastic constitutive laws to account for the finite extensibility of polymer chains (Peterlin 1961; Larson 1988). Further investigation into various microscopic aspects of the C-S transition, involving calibrating the effective conformational energy (Schroeder, Shaqfeh & Chu 2004), determining the threshold of molecular weight (Hsieh & Larson 2005) and studying the characteristic post-extension relaxation time (Doyle *et al.* 1998) and ergodicity-breaking mechanisms in model reduction (i.e. from polymer chain to dumbbell, Beck & Shaqfeh 2007), were extensively explored using Brownian dynamics simulations based on beads-spring-chain models, which accounted for bead–bead hydrodynamic interactions.

In a broader context, abrupt configurational transitions have often been observed in microfluidic systems where various thin elastic structures of much larger sizes than polymer molecules interact with strong viscous flows. For example, a fluid vesicle (Kantsler, Segre & Steinberg 2008; Narsimhan, Spann & Shaqfeh 2015; Kumar, Richter & Schroeder 2020) under extension can exhibit sharp transitions from tubular to dumbbell shapes. More interestingly, a thin elastic sheet of different shapes in elongational flows may undergo a 'compact-stretched' transition with hysteresis, akin to the C-S transition of polymer molecules (Silmore, Strano & Swan 2021; Yu & Graham 2021, 2022). As demonstrated by Yu & Graham (2021, 2022), who performed direct simulation of flexible sheets in flows, successfully achieving C-S transition at the macro scale requires the use of finite-extensibility elastic models, such as the Yeoh elastic model (Yeoh 1993).

The intriguing aspect of cross-scale observations of C-S transitions is that they indicate the existence of specific universal hydrodynamic coupling mechanisms for a class of problems involving interactions between fluids and elastic structures. These mechanisms are applicable to small polymer molecules but are independent of the stochastic nature of the microsystem. In fact, Hinch (1974, 1977) previously suggested the possibility of connecting the chain unfolding process to the stretching deformation of a homogeneous ellipsoidal elastic particle (EP), a reduced-order mechanical model for dilute, coiled polymers and was initially introduced by Cerf (1952) and later extended by Roscoe (1967). Compared with stochastic kinetic models for elastic dumbbells or bead-spring chains, the EP model is mathematically simpler and has much fewer degrees of freedom, and naturally captures the shape-dependent hydrodynamic effects that become increasingly dominant in strong flows. But the EP model cannot represent polymer chains since it oversimplifies the intricate heterogenous coiled microstructures, and ignores the stochastic features such as Brownian forces.

Although the early models (Cerf 1952; Goddard & Miller 1967; Roscoe 1967) successfully accounted for shape-dependent fluid forces, their simple elastic constitutive laws (e.g. linear or neo-Hookean elastic model) fail to describe the constitutive relation at high strains, making them incapable of capturing hysteresis phenomena. Recognizing this limitation, the natural progression, as also suggested by Hinch (1977), is to incorporate different nonlinear constitutive laws to mimic polymer chain's finite extensibility in strong flows. Continuing along this line of investigation, in this study we present an improved EP model to investigate the C-S transition of polymer molecules. Despite having been proposed several decades ago, the precise mathematical formulation of the EP model incorporating finite extensibility has yet to be thoroughly examined. Here we employ an analytical approach originally derived by the author (Gao, Hu & Ponte Castañeda 2011, 2012, 2013) to describe EP deformation. The method utilizes the polarization technique (Eshelby 1957, 1959; Willis 1981) to derive an exact solution for the isolated nonlinear EP problem under simple Stokes flow conditions (i.e. flows with constant velocity gradients). To account for finite and large deformation behaviours, we employ the incompressible Gent hyperelastic model (Gent 1996; Avazmohammadi & Ponte Castañeda 2015), which captures significant strain hardening at large strains. As demonstrated below, this new model unveils the elastohydrodynamics of the C-S transition in uniaxial elongational flows, regulated by finite extensibility, and robustly captures hysteresis phenomena that are akin to polymer chain behaviours. It is worth emphasizing that the Gent model was chosen primarily due to its simple two-parameter form, facilitating analytical manipulations. We have also tested other similar strain-hardening models, such as the Yeoh model (Yeoh 1993), which qualitatively captures similar transition behaviours. Additionally, we can explain the system's bistability through a free-body diagram at steady state without relying on dynamic properties (e.g. relaxation time) of polymer chains. Furthermore, the model allows for convenient extraction of other analytical features, such as the sharpness of the transition region, and enables systematic examination of their dependencies on material and geometric parameters, including stiffness, flow rate and initial shapes.

The structure of the paper is outlined as follows. In § 2 we provide a concise overview of the polarization method based on Eshelby's solution and derive the condition for the steady-state deformation of a Gent EP under uniaxial extension. Section 3 focuses on examining the characteristic steady-state solutions and unveiling the C-S transition phenomenon by monitoring the principal stretch of the semi-major axis of the spheroid as the flow strength increases. Moreover, we elucidate the physical mechanisms behind the observed hysteresis behaviours through force-balance analysis. In addition, we have

also investigated the use of alternative constitutive laws, such as the Yeoh hyperelastic model, which accounts for the strain-hardening effect, and observed similar C-S transition behaviours. Finally, some conclusions are drawn in § 4.

2. Mathematical model

Our study focuses on investigating the dynamics of a long-chain polymer that is initially coiled and exposed to an unbounded, uniaxial three-dimensional elongational flow $(\dot{\gamma}x_1, -(\dot{\gamma}/2)x_2, -(\dot{\gamma}/2)x_3)$ with constant flow rate $\dot{\gamma}$. In our approach, rather than explicitly modelling the intricate details of the flexible chains, we approximate the polymer as an isotropic, incompressible EP. This particle is assumed to possess an ellipsoidal shape that instantaneously adjusts to the flow conditions and exhibits a no-slip surface, as depicted in figure 1. In the limit of a vanishingly small Reynolds number ($Re \to 0$), the continuity and momentum equations can be expressed in a coherent manner throughout the entire domain as

$$\boldsymbol{\nabla} \cdot \boldsymbol{v} = 0 \quad \text{and} \quad \boldsymbol{\nabla} \cdot \boldsymbol{\sigma} = \boldsymbol{0}. \tag{2.1a,b}$$

In the Eulerian fluid domain Ω_f (denoted by subscript 'f'), the total stress tensor $\boldsymbol{\sigma}_f$ is defined by the constitutive relation

$$\boldsymbol{\sigma}_f = -p_f \boldsymbol{I} + 2\mu \boldsymbol{D}_f, \tag{2.2}$$

where μ is the fluid viscosity, p_f is the pressure and $\boldsymbol{D}_f = \frac{1}{2}(\boldsymbol{\nabla v} + \boldsymbol{\nabla v}^{\mathrm{T}})$ is the rate-of-deformation or strain-rate tensor. Likewise, in the solid particle domain Ω_s (denoted by the subscript 's'), we define

$$\boldsymbol{\sigma}_s = -p_s \boldsymbol{I} + \boldsymbol{\tau}, \tag{2.3}$$

where p_s is a pseudo-pressure, serving as a Lagrangian multiplier to enforce the incompressibility constraint. In general, the extra solid stress $\boldsymbol{\tau}$ can be defined as a function of the Finger (or left Cauchy–Green) tensor $\boldsymbol{B} = \boldsymbol{F}\boldsymbol{F}^T$, with $\boldsymbol{F} = \partial \boldsymbol{x}/\partial \boldsymbol{X}$ denoting the deformation gradient tensor, where $\{\boldsymbol{x}\}$ and $\{\boldsymbol{X}\}$ denote the current and reference domain, respectively. For a neo-Hookean solid with the shear modulus η, the extra stress is taken as $\boldsymbol{\tau} = \eta(\boldsymbol{B} - \boldsymbol{I})$, which permits infinite strain. For the purpose of modelling solids with finite extensibility, we have opted to utilize the incompressible Gent model whose constitutive relation can be written as

$$\boldsymbol{\tau} = \eta\left(1 - \frac{I_1 - 3}{J}\right)^{-1} (\boldsymbol{B} - \boldsymbol{I}) = \eta\chi\,(\boldsymbol{B} - \boldsymbol{I})\,, \tag{2.4}$$

which is derived from an elastic potential energy $W = -(\eta J/2)\ln(1 - (I_1 - 3)/J)$ (Gent 1996; Avazmohammadi & Ponte Castañeda 2015). Notably, the prefactor $\chi = (1 - (I_1 - 3)/J)^{-1}$ in the equation signifies the finite extensibility of the polymer chain, where I_1 is the so-called first invariant of the Cauchy strain tensor. Besides η, the only new parameter, the strain limit constant $J > 0$, determines the maximum allowable values for the principal stretches. It is evident that the elastic stress $\boldsymbol{\tau}$ will become unbounded as I_1 approaches the upper limit of $J + 3$, effectively capturing the strain-hardening behaviour. When $J \to \infty$ is chosen, the Gent model automatically recovers the neo-Hookean model without enforcing stiffening at large strain. The rate of change of $\boldsymbol{B}$ satisfies the evolution

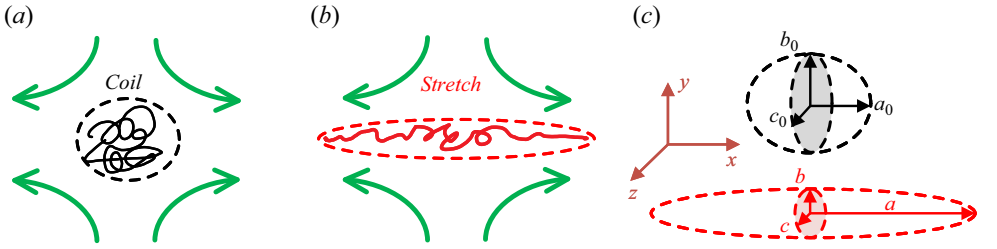

Figure 1. Schematic of the EP model for C-S transition of an initially coiled long-chain polymer. The spheroidal envelop with the semi-axes $a_0 \geqslant b_0 = c_0$ will deform axisymmetrically into a more slender shape at the steady state.

equation (Joseph 1990)

$$\frac{\mathrm{D}\boldsymbol{B}}{\mathrm{D}t} = \boldsymbol{\nabla v}^T \cdot \boldsymbol{B} + \boldsymbol{B} \cdot \boldsymbol{\nabla v}, \tag{2.5}$$

where $\mathrm{D}/\mathrm{D}t = \partial/\partial t + (\boldsymbol{v} \cdot \boldsymbol{\nabla})$ denotes a material time derivative. The set of governing equations (2.1*a*,*b*)–(2.5), along with the velocity and traction continuity conditions at the fluid–solid interface, will be simultaneously solved. To non-dimensionalize the above equations, we have chosen the characteristic length scale as the particle size d_p, the time scale $\dot{\gamma}^{-1}$, the velocity scale $\dot{\gamma} d_p$ and the pressure and stress scale $\mu\dot{\gamma}$. The elastic deformation is characterized by the shear modulus η. Hence, the dimensionless parameter defined as $G = \mu\dot{\gamma}/\eta$ measures the viscous force in the fluid relative to the elastic force in the solid, and hence, can be termed as an effective 'stretching' parameter that characterizes the magnitude of the elastic stretching deformation subjected to the elongational flow field.

The polarization method developed by Gao *et al.* (2011), derived from the classical Eshelby problem in composite materials (Eshelby 1957, 1959), offers additional analytical tools for manipulating the aforementioned fluid–solid system. This method leverages the insight that a uniform (yet potentially time-dependent) strain rate and vorticity fields within the particle indicate that the particle undergoes a series of transformations into ellipsoidal shapes before reaching a final steady state (Goddard & Miller 1967; Roscoe 1967; Bilby, Eshelby & Kundu 1975; Bilby & Kolbuszewski 1977; Hinch 1977; Ogden 1984; Wetzel & Tucker 2001). The key step is introducing a uniform, incompressible 'reference' medium for the solid phase with the same viscosity μ_f as the fluid phase, and define the dimensionless stress polarization tensor $\boldsymbol{\Xi}$ as the total stress difference, or 'polarization tensor'

$$\boldsymbol{\Xi} = \boldsymbol{\sigma} + p\boldsymbol{I} - 2\boldsymbol{D}. \tag{2.6}$$

Here we have dropped the subscripts 'f' and 's' in the definition so that the governing equations can be universally constructed in the entire domain as

$$\boldsymbol{\nabla} \cdot \boldsymbol{v} = 0, \quad \nabla^2 \boldsymbol{v} - \boldsymbol{\nabla} p + \boldsymbol{\nabla} \cdot \boldsymbol{\Xi} = \boldsymbol{0}, \tag{2.7a,b}$$

which can be reinterpreted as an equivalent problem for the homogeneous reference medium subjected to a distribution of body force $\boldsymbol{\nabla} \cdot \boldsymbol{\Xi}$ in the particle. Hence, the solution of the velocity field $\boldsymbol{v}$ of the forced Stokes equation in (2.7*a*,*b*) can be represented as

$$\boldsymbol{v}(\boldsymbol{x}) = \boldsymbol{L}^0 \cdot \boldsymbol{x} + \int_{\Omega_s} \boldsymbol{G}^0(\boldsymbol{x}, \boldsymbol{x}') \cdot (\boldsymbol{\nabla}_{\boldsymbol{x}'} \cdot \boldsymbol{\Xi}) \mathrm{d}\boldsymbol{x}', \tag{2.8}$$

where the volume integral is performed over the solid domain Ω_s, $\boldsymbol{L}^0$ represents the imposed far-field velocity gradient and $\boldsymbol{G}^0(\boldsymbol{x}, \boldsymbol{x}')$ is the free-space Green's function or

Stokeslet. By rewriting the tensor $\boldsymbol{G}^0$ in the Fourier space and applying on the uniform forcing field, the strain-rate tensor $\boldsymbol{D}_s = \frac{1}{2}(\boldsymbol{\nabla v} + \boldsymbol{\nabla v}^{\mathrm{T}})$ and the vorticity tensor $\boldsymbol{W}_s = \frac{1}{2}(\boldsymbol{\nabla v} - \boldsymbol{\nabla v}^{\mathrm{T}})$ are found to be given by

$$\boldsymbol{D}_s = (\mathbb{I} - 2\mathbb{P})^{-1} : (\boldsymbol{D}^0 - \mathbb{P} : \boldsymbol{\tau}), \tag{2.9}$$

$$\boldsymbol{W}_s = \boldsymbol{W}^0 - \mathbb{R} : \boldsymbol{\tau} + 2\mathbb{R} \cdot ((\mathbb{I} - 2\mathbb{P})^{-1} : (\boldsymbol{D}^0 - \mathbb{P} : \boldsymbol{\tau})). \tag{2.10}$$

In the above, $\mathbb{I}$ is the fourth-order identity tensor, $\mathbb{P}$ and $\mathbb{R}$ (see results for spheroidal particles in Appendix A) are two fourth-order tensors related to the instantaneous shape of the particle, $\boldsymbol{D}^0 = \frac{1}{2}(\boldsymbol{L}^0 + (\boldsymbol{L}^0)^{\mathrm{T}})$ and $\boldsymbol{W}^0 = \frac{1}{2}(\boldsymbol{L}^0 - (\boldsymbol{L}^0)^{\mathrm{T}})$ are the background strain-rate and vorticity tensors. The readers are referred to more derivation details in Gao *et al.* (2011). It should be pointed out that our definition of the shape tensors is different from the classical Eshelby tensors in solid mechanics literature (Eshelby 1957, 1959; Wetzel & Tucker 2001, see also Willis (1981) and Ponte Castañeda (2005) for more discussion on these choices). Another direct implication of this is that all the spatial gradients on the stress (or strain) fields in the equations, such as the convective term in (2.5), vanishes automatically. With (2.9) and (2.9), the original coupled partial differential equations now convert to a systems of ordinary differential equations for solving the time-dependent (uniform) solid stress and particle shape regarding the aspect ratios and orientation.

In a uniaxial extensional flow, we consider an EP that initially possesses a spheroidal shape (with $a_0 \geqslant b_0 = c_0$), and the semi-major axis is aligned with the x axis. When subjected to uniaxial fluid loading, the EP will deform axisymmetrically into another thinner spheroidal shape ($a > b = c$) with the aspect ratio $\omega = b/a = c/a$. Thus, in the limit case of a spherical particle shape, denoted as $\omega = 1$, it represents a polymer in a perfectly coiled state. Conversely, as ω approaches 0, it corresponds to a fully stretched polymer. The principal stretches of elastic deformation can be written as

$$\lambda_1 = \left(\frac{\omega}{\omega_0}\right)^{-2/3}, \quad \lambda_2 = \lambda_3 = \left(\frac{\omega}{\omega_0}\right)^{1/3}, \tag{2.11a,b}$$

where $\omega_0 = b_0/a_0$ is the initial aspect ratio. Following the definition in (2.4), together with the condition of volume incompressibility of an EP (i.e. $a_0 b_0 c_0 = abc$, or $a_0 b_0^2 = ab^2$ for a spheroid), it is straightforward to obtain the expressions for the three stress components as

$$\tau_{11} = \frac{\chi}{G}(\lambda_1^2 - 1) = \frac{1}{G}\left(1 - \frac{I_1 - 3}{J}\right)^{-1}\left(\left(\frac{\omega}{\omega_0}\right)^{-4/3} - 1\right), \tag{2.12}$$

$$\tau_{22} = \tau_{33} = \frac{\chi}{G}(\lambda_2^2 - 1) = \frac{1}{G}\left(1 - \frac{I_1 - 3}{J}\right)^{-1}\left(\left(\frac{\omega}{\omega_0}\right)^{2/3} - 1\right). \tag{2.13}$$

Here it is important to highlight that utilizing the principal strain λ_i defined in (2.11*a*,*b*) to evaluate the first invariant I_1 in (2.4) is inaccurate. On the one hand, the geometric constraint defined in the prefactor χ entails setting a limit on the maximum attainable length of a fully extended chain, and this limit should not depend on the initial aspect ratio ω_0. On the other hand, the unconstrained part of (2.4), i.e. the Hookean stress–strain relation, requires using the strain that is defined based on the initial configurations that may become partially unfolded already (i.e. $\omega_0 > 0$). Thus, when determining the value of I_1 in χ, we opt to consistently compare the deformed shape to that of a spherical shape,

i.e. fixing $\omega_0 = 1$ for a perfectly coiled shape, and evaluate I_1 using a set of 'reference' principal strain (denoted by superscript '(r)') as

$$I_1 = I_1^{(r)} = \sum_{i=1}^{3} (\lambda_i^{(r)})^2 = \omega^{-4/3}(1 + 2\omega^2), \tag{2.14}$$

with

$$\lambda_1^{(r)} = \omega^{-2/3}, \quad \lambda_2^{(r)} = \lambda_3^{(r)} = \omega^{1/3}. \tag{2.15a,b}$$

Since the particle will not rotate during the symmetric extension, i.e. $\boldsymbol{W}_s = \boldsymbol{0}$ automatically satisfied, the steady-state solution only requires

$$\boldsymbol{D}_s = \boldsymbol{0} \tag{2.16}$$

in (2.9).

3. Results and discussion

Applying the imposed background strain-rate tensor $\boldsymbol{D}^0 = \mathrm{diag}\{1, -1/2, -1/2\}$ and the stress components in (2.16), after some algebraic manipulations, we are able to solve the stretching parameter G as a function of the steady-state aspect ratio $\omega = \Omega$ as

$$G = \frac{J(\Omega^2 - \omega_0^2)\left(\left(\dfrac{\Omega^2 + 2}{\sqrt{1 - \Omega^2}}\right) \ln\left(\dfrac{1 - \sqrt{1 - \Omega^2}}{1 + \sqrt{1 - \Omega^2}}\right) + 6\right)}{4\omega_0^{2/3}(1 - \Omega^2)^2[(J + 3)\,\Omega^{-2/3} - 2 - \Omega^{-2}]}. \tag{3.1}$$

(Or, equivalently, we can numerically solve Ω as a function of G.) In the limit of $J \to \infty$, the above equation reduces to the neo-Hookean case where

$$G = \frac{(\Omega^2 - \omega_0^2)\left(\left(\dfrac{\Omega^2 + 2}{\sqrt{1 - \Omega^2}}\right) \ln\left(\dfrac{1 - \sqrt{1 - \Omega^2}}{1 + \sqrt{1 - \Omega^2}}\right) + 6\right)}{4(\omega_0/\Omega)^{2/3}(1 - \Omega^2)^2}. \tag{3.2}$$

Subsequent analyses and discussions will rely on these fundamental solutions as the basis for further examination. As shown in figures 2(*a*)–2(*c*), the hysteretic C-S transition behaviours are captured when plotting the steady-state value of the principal stretch (i.e. square root of the principal strain) along the semi-major axis against G, corresponding to the scenarios of changing the effective particle stiffness (or, increasing the flow strength). Here we examine two types of strain measurements, namely the actual strain $\Lambda = (\Omega/\omega_0)^{-2/3}$ in (2.11*a*,*b*) and the reference strain $\Lambda^{(r)} = \Omega^{-2/3}$ defined in (2.15*a*,*b*). The discrepancy lies in the fact that Λ quantifies the deformation relative to the initial state, which can possess different shapes (i.e. $0 < \omega_0 \leqslant 1$), whereas $\Lambda^{(r)}$ exclusively measures the deformation relative to a reference spherical shape (i.e. fixing $\omega_0 = 1$). Consequently, the maximum value of $\Lambda^{(r)}$ effectively signifies the finite length of a fully stretched polymer, and is independent of the initial state.

For both types of strain definitions, we can identify two branches of solutions, respectively marked as the 'C' and 'S' state. The S solution branch characterizes the strain-hardening effect, i.e. producing larger elastic deformation to counterbalance the increasing fluid extensional force, which is obviously missing in the neo-Hookean model. In panel (*a*) we fix the initial shape to be spherical so that $\Lambda = \Lambda^{(r)}$, and vary the

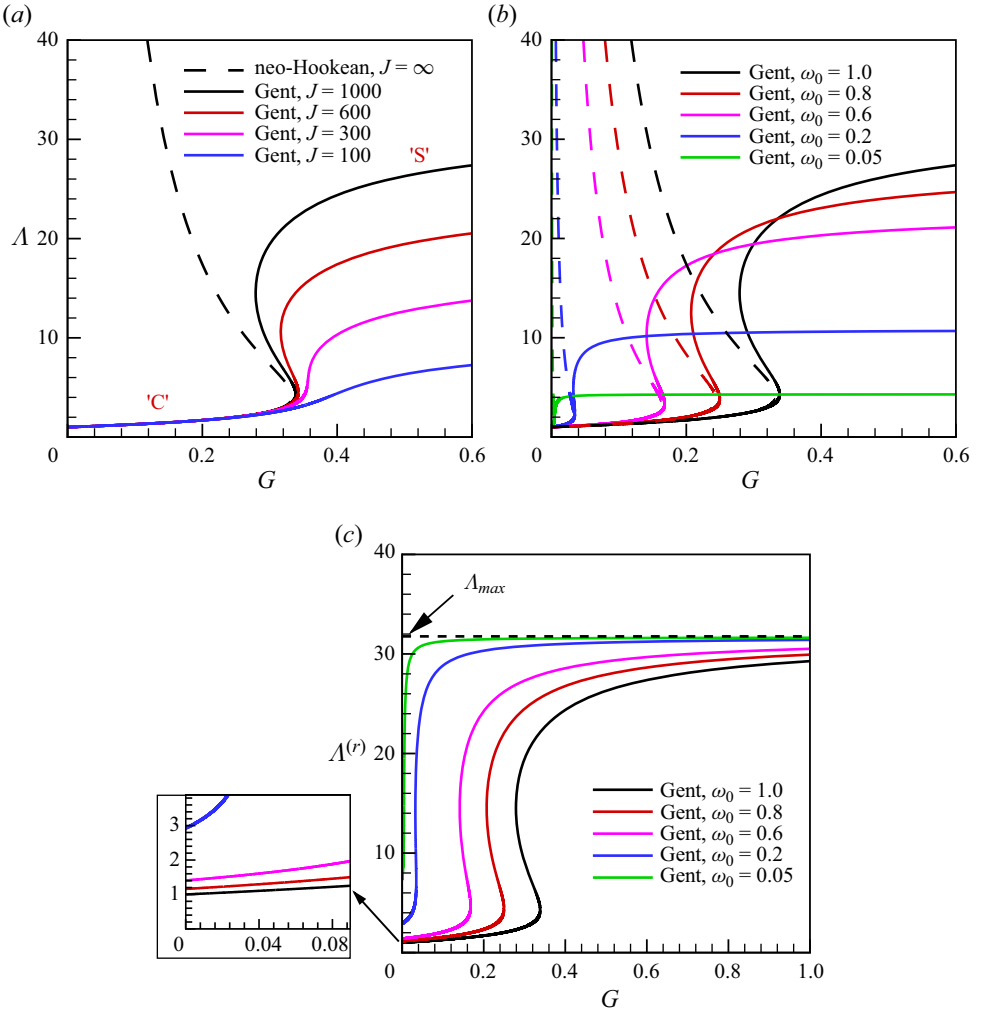

Figure 2. Principal stretch of the semi-major axis as a function of stiffness G for (a) an initially spherical particle $\omega_0 = 1$ with different values of J, and (b,c) an initially spheroidal particle when choosing $0 < \omega_0 \leqslant 1$ and fixing $J = 1000$. In panels (a,b) the dashed line recovers the neo-Hookean model that was previously obtained by Gao *et al.* (2011) and Roscoe (1967). The principal stretch is measured with respect to the actual initial shape (Λ in panel b) and with respect to the reference spherical shape ($\Lambda^{(r)}$ in panel c). In panel (c) the inset shows the zoom-in view in the vicinity of $G = 0$.

strain limit value J. The C-S transition exhibits a relatively smooth and nearly monotonic behaviour for small values of J. However, as J surpasses approximately 300, the transition becomes sudden and exhibits hysteresis. As J continues to increase towards infinity, the C-S transition progressively diminishes due to the Gent model converging towards the neo-Hookean model. This trend is illustrated by the black dashed line, which corresponds to the previous results obtained by Roscoe (1967) and Gao *et al.* (2013). In panel (b) we fix $J = 1000$ and examine the initial shape effect by varying ω_0. As anticipated, initiating the process from a more elongated shape or a pre-stretched configuration leads to an earlier occurrence of the C-S transition, particularly at lower values of G. Moreover, the transition demonstrates a sharper progression towards a fully stretched configuration,

which is consistent with experimental observations for DNAs (Smith & Chu 1998). If the initial spheroidal shape is already considerably thin, only an S branch is present (illustrated by the green curve computed at $\omega_0 = 0.05$), indicating an immediate transition to a fully stretched shape. Moreover, the dashed lines representing the neo-Hookean cases for non-spherical shapes consistently demonstrate a single C state without any transition. In panel (c) we analyse the measurement of the reference strain $\Lambda^{(r)}$ for the same cases as presented in panel (b). The inset on the left provides a zoom-in visual representation of the EP undergoing deformation from various initial shapes, or 'stressless' configurations, characterized by different values of $\Lambda^{(r)}$ at $G = 0$. All S curves are seen to saturate at the maximum allowable strain Λ_{max} which, by definition, can be obtained by directly solving the geometric constraint

$$\Lambda_{max}^2 + \frac{2}{\Lambda_{max}} = J + 3, \tag{3.3}$$

suggesting that the chain eventually unfolds to the same maximum length set by J (Horgan 2015).

Next, we seek a more quantitative characterization of the hysteresis regime during the transition. As shown by the inset of figure 3(a), the extent of the hysteresis region in figure 2 can be determined by measuring the two turning points on the $\Lambda - G$ curves, namely G_{min} and G_{max}, which are obtained by solving the roots of equation

$$\left.\frac{\mathrm{d}G}{\mathrm{d}\Omega}\right|_{\Omega=\Omega_c} = 0 \tag{3.4}$$

from (3.1). In panel (a) we plot G_{max} and G_{min} as functions of the initial aspect ratio ω_0 at different values of J. Evidently, the hysteresis region generally appears narrower at lower values of ω_0 and J, indicating a more abrupt transition. (The zoomed-in view within the inset highlights a particularly rapid transition at $J = 400$.) On the contrary, as the value of J increases, the transition region expands gradually, whereby the upper limit G_{max} approaches the neo-Hookean case, and the lower limit G_{min} decreases. Another intriguing observation is that for initially spherical shapes at $\omega_0 = 1$, a consistent value of $G_{max} \approx 0.34$ is maintained across all large and finite values of J ($J > 300$) when two turning points are present, and hence, serves as a global maximum. This result even aligns with the findings for initially circular elastic sheets undergoing C-S transition in elongational flows using the Yeoh hyperelastic model (Yu & Graham 2021). In panel (b) we plot the steady-state aspect ratio $\Omega_c = \Omega_{min}$ and $\Omega_c = \Omega_{max}$ that corresponds to G_{max} and G_{min}, respectively. With increasing J, the upper limit tends to converge towards the neo-Hookean case, whereas the lower limit diminishes to zero. In panel (c) we gather data for the 'thinnest' initial shape, represented by $\omega_0 = \omega_0^*$, as a function of J that can induce hysteresis. Mathematically, these instances correspond to the stationary reflection points on the $\Lambda - G$ curves, resulting in the merging of the two bounds in panel (b), denoted as $\Omega_c = \Omega_{min} = \Omega_{max}$. For all the cases considered, we identify a global minimum $J_{min} \approx 330$ as $\omega_0^* \to 1$ for initially spherical EPs.

To understand the underlying mechanism behind the hysteresis behaviour captured by the EP model, we employ the analysis approach introduced by Gao *et al.* (2013) to examine the force balance of the half-spheroid, as depicted in figure 4. When subjected to a simple uniaxial elongation field, the deformation of the EP is primarily governed by the interplay between external hydrodynamic forces and internal elastic resistance forces along the x axis. We utilized the fundamental solutions for a rigid ellipsoidal particle moving in Stokes flows derived by Jeffery (1922) to calculate the horizontal fluid extensional force exerted

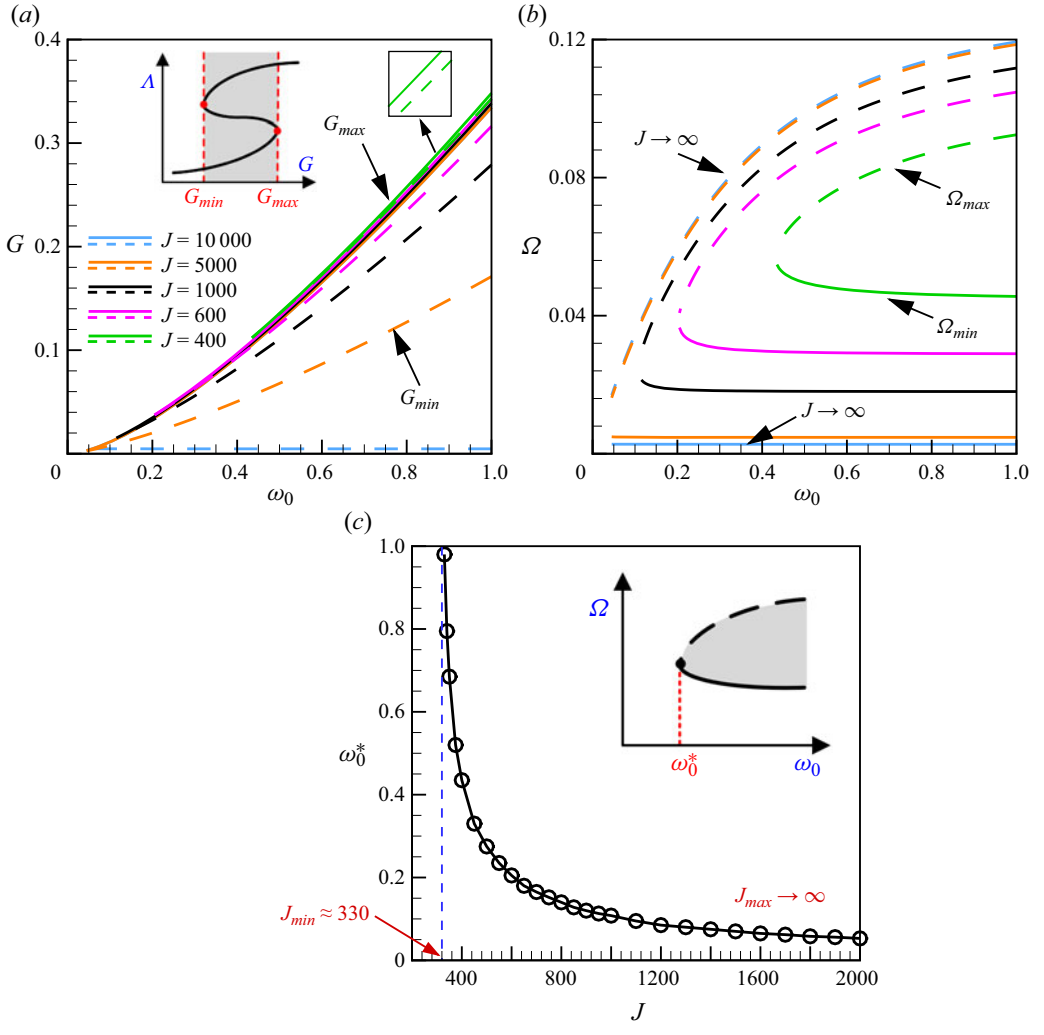

Figure 3. Phase diagrams for computational parameters to characterize hysteresis. (*a*) The width of the hysteretic regime featured by the distance between the turning points of the $G-\Lambda$ curves. The upper (G_{max}, marked by solid lines) and lower (G_{min}, marked by dashed lines) bounds as a function of initial aspect ratio ω_0 at some typical values of J. (*b*) The corresponding values of Ω_{min} (for G_{max}) and Ω_{max} (for G_{min}) as functions of ω_0. (*c*) The minimum initial aspect ratio ω_0^* for hysteresis to occur as a function of J.

on the particle surface ∂S_h as

$$F_{fluid} = \oint_{\partial S_h} \hat{\boldsymbol{e}}_1 \cdot (\boldsymbol{\sigma}_f \cdot \boldsymbol{n}) \mathrm{d}S, \tag{3.5}$$

where $\hat{\boldsymbol{e}}_1$ is the unit vector along the x axis. The external fluid force is counterbalanced by the internal elastic force exerted upon the middle cross-section of the particle. Since the stress and strain fields in the particle are uniform, the responsive force $F_{elastic}$ can be then simply expressed as

$$F_{elastic} = (\boldsymbol{\sigma}_s \cdot \hat{\boldsymbol{e}}_1) \times A, \tag{3.6}$$

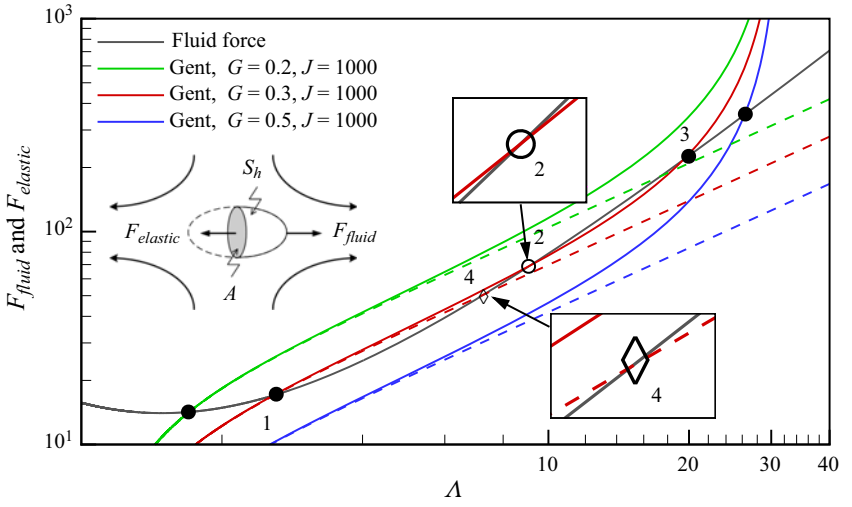

Figure 4. Force balance of the half-spheroidal EP revealing the physical mechanism of hysteresis. Both the Gent (solid lines) and the neo-Hookean (dashed lines) models are tested for initially spherical EP, i.e. $\omega_0 = 1$ for some typical values of G. Inset: free-body diagram of the half-spheroid. The filled and open symbols mark the stable and unstable equilibrium states, respectively.

where $A = \pi b^2$ is the surface area. It is important to note a subtle point in our analysis. We choose to evaluate the deviatoric component of the fluid stress, denoted as $\boldsymbol{\sigma}_f = 2\boldsymbol{D}_f$, and incorporate the pressure difference between the two phases into the solid stress, denoted as $\boldsymbol{\sigma}_s = -(p_s - p_f)\boldsymbol{I} + \boldsymbol{\tau}$. This choice allows us to eliminate the arbitrary reference pressure. Furthermore, this approach has the advantage of making the fluid force F_{fluid} solely dependent on the shape of the EP, while the elastic force $F_{elastic}$ is influenced by various factors including the EP's shape, stiffness and strain limit.

Theoretically, F_{fluid} and $F_{elastic}$ must balance in steady states. As depicted in figure 4, where we keep the initial shape $\omega_0 = 1$ and strain limit $J = 1000$, hysteresis can be observed based on the phase diagrams shown in figure 3. The steady-state solutions are obtained by determining the intersections of the two functions, $F_{fluid}(\Omega)$ (represented by the black solid line) and $F_{elastic}(\Omega, G)$. The number of intersections directly indicates the characteristic properties of the C-S transition. When choosing a small G (e.g. $G = 0.2$ marked as a green line), there is only one intersection, corresponding to the solutions on the C branch of the $\Lambda - G$ curves in figure 2. Similarly, for a large value of G (e.g. $G = 0.5$ indicated by the blue line), the presence of a single intersection corresponds to the S branch of the transition. Nevertheless, if we select a value of G within the transition regime defined by $G \in [G_{min}, G_{max}]$ as shown in figure 3, we can observe three intersections along the red line. From left to right, these intersections are labelled as states 1, 2 and 3 in figure 4. Let us focus on state 1 located on the C branch. If Ω decreases (increases) slightly from the intersection point (i.e. the particle becomes slightly more elongated), $F_{elastic}$ becomes larger (smaller) than F_{fluid}, causing the EP to contract (stretch) correspondingly to restore the equilibrium configuration. The same conceptual analysis applies to state 3 on the S branch. Therefore, both of these equilibrium solutions are stable and indicated by filled circles. In contrast, applying the same analysis to state 2 represented by an open circle reveals an opposite trend. When Ω slightly decreases (increases), $F_{elastic}$ becomes smaller (larger) than F_{fluid}, causing the EP to continue extensional (contracting) without reaching equilibrium. At this point, a numerical linear stability analysis could be employed

to characterize the system behaviour quantitatively and more rigorously. However, we find that the bistability analysis described above, although simplistic, is intuitive and straightforward. It also aligns with the earlier kinetic models (DeGennes 1974; Hinch 1974, 1977; Fuller & Leal 1980), and reflects the essence of the phenomenological double-well potential. As comparisons, we investigate the corresponding cases under the neo-Hookean model, seen as the dashed lines. As anticipated, no bistable solutions are observed, and only a stable C branch exists. Additionally, we have identified a second class of equilibrium solutions, referred to as state 4 and denoted by the open diamond, during the transition. However, just like state 2, it is evident that these solutions are determined to be unstable.

Finally, we conduct an additional verification to confirm the validity of the physical mechanisms identified above. Instead of utilizing the Gent model, we employ the Yeoh model (Yeoh 1993), which is another widely used nonlinear hyperelastic model that incorporates strain hardening. The incompressible Yeoh model is characterized by a constitutive relation with a three-parameter form

$$\tau_{11} = \frac{1}{G}(1 + z_1(I_1 - 3) + z_2(I_1 - 3)^2)\left(\left(\frac{\omega}{\omega_0}\right)^{-4/3} - 1\right), \tag{3.7}$$

$$\tau_{22} = \tau_{33} = \frac{1}{G}(1 + z_1(I_1 - 3) + z_2(I_1 - 3)^2)\left(\left(\frac{\omega}{\omega_0}\right)^{2/3} - 1\right), \tag{3.8}$$

with $z_{1,2}$ the material constants ($z_{1,2} = 0$ reduces to the neo-Hookean model). As shown in figure 5, when selecting suitable values for the parameters $z_{1,2}$ in the Yeoh model, an EP governed by the Yeoh model demonstrates hysteresis in the C-S transition when measuring the principal stretch, which bears qualitative similarities to the hysteresis observed in a Gent EP. It is noteworthy that the Yeoh model, which does not impose a restriction on the maximum strain, exhibits generally smoother stiffening behaviours at high strains. In panel (*b*) we demonstrate that by simultaneously adjusting two parameters, more versatile control over the stiffening behaviours at high strains can be achieved compared with using a single-parameter form in (2.12) and (2.13). The impact of the initial shape is investigated in panel (*c*), where similar trends to the Gent model are observed, i.e. the transition becomes sharper for thinner shapes and the global maximum $G_{max} \approx 0.34$ when choosing $\omega_0 = 1$. A closer examination in panel (*d*) reveals that the equilibrium solutions on the lower C branch, including the turning points for different ω_0, are nearly independent of the specific model used. This is because all these nonlinear models accurately capture small and finite elastic deformations. Consequently, the simple neo-Hookean model should accurately predict the C states, while the S states may exhibit some variations when different models are employed.

4. Conclusion

We have presented an EP model with finite extensibility to restudy the C-S transition of dilute polymers under steady elongational flows. Unlike previous kinetic models that were developed for weak flows with *ad-hoc* hydrodynamic adjustments, our model directly addresses the elastohydrodynamics in the strong flow limit. Additionally, we have employed the Gent hyperelastic model, which is a simple nonlinear constitutive model capable of capturing the strain-hardening effect, to replicate the finite extensibility of polymer chains. Drawing inspiration from microscopic models and simulations, we have characterized the shape change of EP by monitoring its principal stretch at the steady state, analogous to the end-to-end distance of a polymer, as a function of the effective stiffness

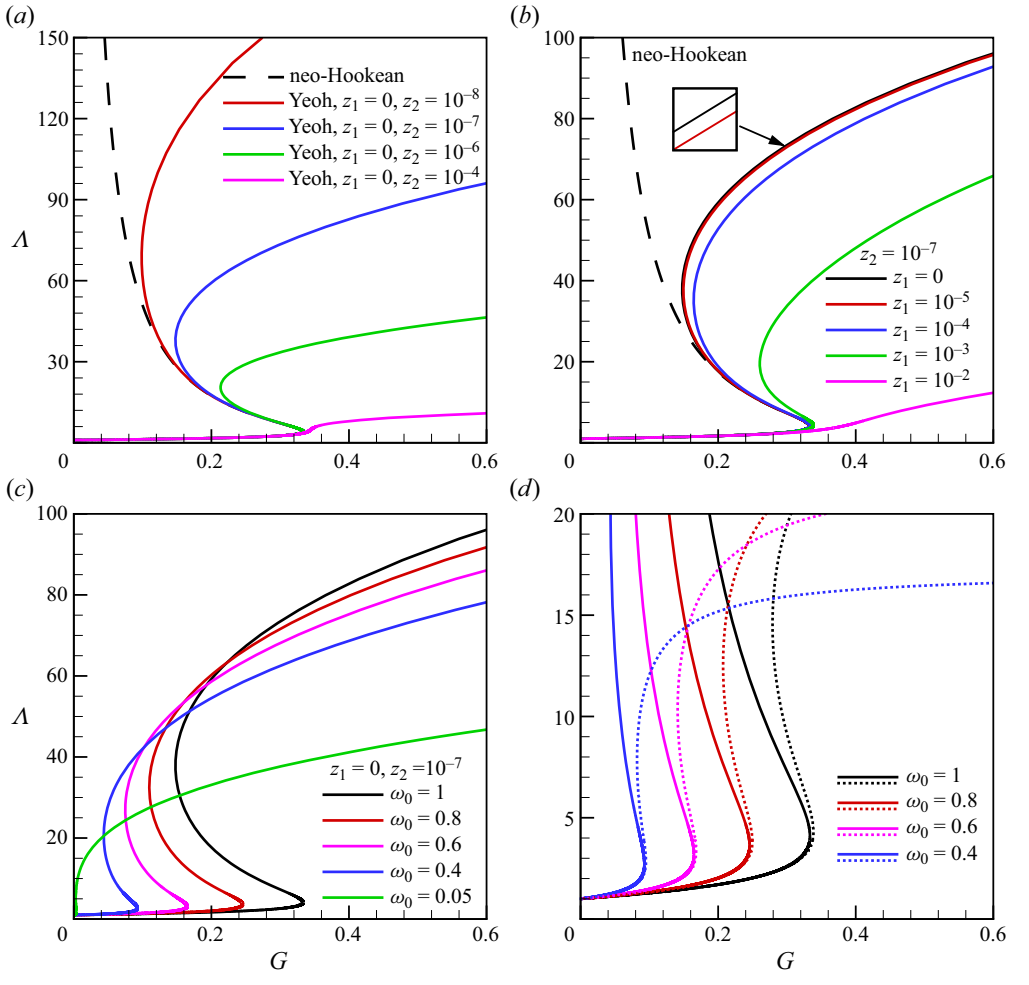

Figure 5. Principal stretch of the semi-major axis as a function of stiffness G for the Yeoh model (Yeoh 1993). (*a*) Initially spherical particle $\omega_0 = 1$ at $z_1 = 0$ and different values of z_2. (*b*) Initially spherical particle $\omega_0 = 1$ at different values of z_1 while fixing $z_2 = 10^{-7}$. (*c*) Spheroidal particle with different ω_0 and fixing $z_1 = 0$ and $z_2 = 10^{-7}$. (*d*) Zoom-in view of the 'C' branch for both the Yeoh (solid lines) and Gent (dotted lines, $J = 1000$) models.

of the particle, which is equivalent to modifying the strength of the flow. Our results have successfully demonstrated that the interplay between shape ellipticity and nonlinear elasticity can generate complex hysteresis phenomena, resembling those observed in the behaviour of single polymers subjected to elongational flows. Furthermore, we have explained the C-S transition of EP by identifying bistable deformations at equilibrium through a force-balance analysis, which connects to the concept of a double-well conformational energy present in stochastic kinetic models. The same analysis can be extended to study the original model by Roscoe (1967) for viscoelastic particles of Kelvin–Voigt type where a viscous term is linearly incorporated in the solid phase.

Although some qualitative behaviours were predicted a long time ago by Hinch (1974, 1977), it is still astonishing to observe that a simplified EP model can capture many intricate details of complex hysteresis phenomena. The transition mechanism appears to be robust, as similar results are obtained using different constitutive models, as

long as the strain-hardening effect is incorporated. Nonetheless, we have found that the incompressible Gent model is particularly appealing. Not only does it possess a simple (possibly the simplest) mathematical formulation, but the value of strain limit J also has a clear geometric interpretation and can potentially be directly calibrated by solving Λ_{max} and comparing with the maximum attainable chain length under extension before chain breakage may occur. For instance, when selecting J around 1000 in the Gent model, we observe that the principal stretch at the S state is approximately of the order of 30–40, which aligns with the results obtained from Brownian dynamics simulations for a long-chain DNA molecule over 1 μm long by Schroeder *et al.* (2004). A similar hysteresis curve can be produced when choosing $z_2 \sim 10^{-7}$–10^{-6} and $z_1 < 10^{-4}$ in the Yeoh model. Therefore, the actual value of J can be selected by carefully comparing $\Lambda^{(r)}$ with the relative extension length measured in simulations. In this regard, the EP model suggests that the C-S transition is more favourable for long-chain polymers, albeit with a finite length (e.g. $J < O(10^4)$). Otherwise, for very long chains, the strain-hardening effects diminish, leading to effectively neo-Hookean behaviour and the absence of hysteresis. It should be noted that the EP model can even capture similar behaviours exhibited by much larger, thin, flexible structures like fibres or sheets in elongational flows. Nevertheless, the model described is limited in its ability to account for more complex material behaviours, such as the buckling instability observed in microfibres flowing in viscous fluids (Cappello *et al.* 2022). The underlying mechanisms rely on the accurate depiction of various wavy deformations exhibited by thin fibres, which surpasses the assumption of ellipticity and homogeneity made in the EP model.

It is intriguing to study critical behaviours of Gent EP in more complex scenarios in mixed flows that linearly combine the rotational and extensional flows (Smith *et al.* 1999; Schroeder *et al.* 2005; Teixeira *et al.* 2005). As demonstrated by Fuller & Leal (1981) and Hoffman & Shaqfeh (2007), consistent capturing of hysteresis has been achieved but the polymer's fractional extension may deviate from that observed in pure extensional flow. This discrepancy is contingent upon the strength of the rotational effect. While the same framework of polarization method could be used, in these general cases, the particle shape loses its axisymmetry, resulting in much more complex shape tensors that cannot be integrated analytically as those derived in Appendix A. Hence, the pursuit of equilibrium solutions for the dynamic systems will involve *ad-hoc* numerical methods for accurate and efficient evaluation of elliptic integrals, proving to be an exceedingly challenging endeavour. Moreover, an initially non-spherical EP will tumble periodically when subjected to shear while simultaneously undergoing stretching or compression (Smith *et al.* 1999; Hur *et al.* 2002; Schroeder *et al.* 2005; Teixeira *et al.* 2005; Hoffman & Shaqfeh 2007), which require assessing the particle deformation via a proper time average. Given these challenges and the large parameter space (two-dimensional and three-dimensional mixed flows, initial aspect ratio and strain limit value), we have chosen to undertake a distinct investigation specifically focusing on linear mixed flows in the future.

Funding. This work is partially supported by the National Science Foundation grant no. 1943759.

Declaration of interests. The author reports no conflict of interest.

Author ORCIDs.
Tong Gao https://orcid.org/0000-0001-5049-8538.

Appendix A. Shape tensors for initially spheroidal particles

For initially prolate spheroidal particles, since the particle shape remains spheroidal during motion, the shape tensors $\mathbb{P}$ and $\mathbb{R}$ can be solved analytically as

$$\left.\begin{aligned}
P_{11} &= \frac{\omega^2\{(\omega^2+2)(\ln\omega - \ln(1-\sqrt{1-\omega^2})) - 3\sqrt{1-\omega^2}\}}{2(1-\omega^2)^{5/2}},\\
P_{22} = P_{33} &= \frac{(5\omega^4+4\omega^2)(\ln\omega - \ln(1-\sqrt{1-\omega^2})) - (11\omega^2-2)\sqrt{1-\omega^2}}{16(1-\omega^2)^{5/2}},\\
P_{12} = P_{13} &= \frac{\omega^2\{(\omega^2+2)(\ln(1-\sqrt{1-\omega^2}) - \ln\omega) + 3\sqrt{1-\omega^2}\}}{4(1-\omega^2)^{5/2}},\\
P_{23} &= \frac{(\omega^4-4\omega^2)(\ln(1-\sqrt{1-\omega^2}) - \ln\omega) - (\omega^2+2)\sqrt{1-\omega^2}}{16(1-\omega^2)^{5/2}},\\
P_{44} &= \frac{6\omega^4(\ln\omega - \ln(1-\sqrt{1-\omega^2})) - (5\omega^2-2)\sqrt{1-\omega^2}}{16(1-\omega^2)^{5/2}},\\
P_{55} = P_{66} &= \frac{3\omega^2(\omega^2+1)(\ln(1-\sqrt{1-\omega^2}) - \ln\omega) + (2\omega^4+3\omega^2+1)\sqrt{1-\omega^2}}{8(1-\omega^2)^{5/2}},\\
R_{55} = R_{66} &= \frac{3\omega^2(\ln\omega - \ln(1-\sqrt{1-\omega^2})) - (2\omega^2+1)\sqrt{1-\omega^2}}{8(1-\omega^2)^{3/2}},
\end{aligned}\right\} \tag{A1}$$

where a contracted index notation (Wetzel & Tucker 2001; Gao *et al.* 2011) is used.

References

Avazmohammadi, R. & Ponte Castañeda, P. 2015 The rheology of non-dilute dispersions of highly deformable viscoelastic particles in Newtonian fluids. *J. Fluid Mech.* **763**, 386–432.

Beck, V.A. & Shaqfeh, E.S.G. 2007 Ergodicity-breaking and the unraveling dynamics of a polymer in linear and nonlinear extensional flows. *J. Rheol.* **51** (3), 561–574.

Bilby, B.A., Eshelby, J.D. & Kundu, A.K. 1975 The change of shape of a viscous ellipsoidal region embedded in a slowly deforming matrix having a different viscosity. *Tectonophysics* **28**, 265–274.

Bilby, B.A. & Kolbuszewski, M.L. 1977 The finite deformation of an inhomogeneity in two-dimensional slow viscous incompressible flow. *Proc. R. Soc. Lond.* A **355**, 335–353.

Bird, R.B. 1987 *Dynamics of Polymeric Liquids, Volume 1: Fluid Mechanics*. Wiley.

Cappello, J., du Roure, O., Gallaire, F., Duprat, C. & Lindner, A. 2022 Fiber buckling in confined viscous flows: an absolute instability described by the linear Ginzburg–Landau equation. *Phys. Rev. Lett.* **129**, 074504.

Cerf, R. 1952 On the frequency dependence of the viscosity of high polymer solutions. *J. Chem. Phys.* **20**, 395–402.

DeGennes, P.G. 1974 *The Physics of Liquid Crystals*. Oxford University Press.

Doyle, P.S., Shaqfeh, E.S.G., McKinley, G.H. & Spiegelberg, S.H. 1998 Relaxation of dilute polymer solutions following extensional flow. Dedicated to the memory of Professor Gianni Astarita. *J. Non-Newtonian Fluid Mech.* **76** (1), 79–110.

Eshelby, J.D. 1957 The determination of the elastic field of an ellipsoidal inclusion and related problems. *Proc. R. Soc. Lond.* A **241**, 376–396.

Eshelby, J.D. 1959 The elastic field outside an ellipsoidal inclusion. *Proc. R. Soc. Lond.* A **252**, 561–569.

Fuller, G.G. & Leal, L.G. 1980 Flow birefringence of dilute polymer solutions in two-dimensional flows. *Rheol. Acta* **19**, 580–600.

Fuller, G.G. & Leal, L.G. 1981 The effects of conformation-dependent friction and internal viscosity on the dynamics of the nonlinear dumbbell model for a dilute polymer solution. *J. Non-Newtonian Fluid Mech.* **8** (3), 271–310.

GAO, T., HU, H.H. & PONTE CASTAÑEDA, P. 2011 Rheology of a suspension of elastic particles in a viscous shear flow. *J. Fluid Mech.* **687**, 209–237.

GAO, T., HU, H.H. & PONTE CASTAÑEDA, P. 2012 Shape dynamics and rheology of soft elastic particles in a shear flow. *Phys. Rev. Lett.* **108**, 058302.

GAO, T., HU, H.H. & PONTE CASTAÑEDA, P. 2013 Dynamics and rheology of elastic particles in an extensional flow. *J. Fluid Mech.* **715**, 573–596.

GENT, A.N. 1996 A new constitutive relation for rubber. *Rubber Chem. Technol.* **69** (1), 59–61.

GODDARD, J.D. & MILLER, C. 1967 Nonlinear effects in a rheology of dilute suspensions. *J. Fluid Mech.* **28**, 657–673.

HINCH, E.J. 1974 Mechanical models of dilute polymer solutions for strong flows with large polymer deformations. In *Proceedings of Colloques Internationaux du Centre de la Recherche Scientifique*, pp. 241–247. Editions du Centro National de la Recherche Scientifique.

HINCH, E.J. 1977 Mechanical models of dilute polymer solutions in strong flows. *Phys. Fluids* **20** (10), S22–S30.

HOFFMAN, B.D. & SHAQFEH, E.S.G. 2007 The dynamics of the coil-stretch transition for long, flexible polymers in planar mixed flows. *J. Rheol.* **51** (5), 947–969.

HORGAN, C.O. 2015 The remarkable gent constitutive model for hyperelastic materials. *Intl J. Non-Linear Mech.* **68**, 9–16.

HSIEH, C.-C. & LARSON, R.G. 2005 Prediction of coil-stretch hysteresis for dilute polystyrene molecules in extensional flow. *J. Rheol.* **49** (5), 1081–1089.

HUNKELER, D., NGUYEN, T.Q. & KAUSCH, H.H. 1996 Polymer solutions under elongational flow: 2. An evaluation of models of polymer dynamics for transient and stagnation point flows. *Polymer* **37** (19), 4271–4281.

HUR, J.S., SHAQFEH, E.S.G., BABCOCK, H.P. & CHU, S. 2002 Dynamics and configurational fluctuations of single DNA molecules in linear mixed flows. *Phys. Rev.* E **66**, 011915.

JEFFERY, G. 1922 The motion of ellipsoidal particles immersed in a viscous fluid. *Proc. R. Soc. Lond.* A **102**, 161–179.

JOSEPH, D.D. 1990 *Fluid Dynamics of Viscoelastic Liquids*. Applied Mathematical Sciences, vol. 84. Springer.

KANTSLER, V., SEGRE, E. & STEINBERG, V. 2008 Critical dynamics of vesicle stretching transition in elongational flow. *Phys. Rev. Lett.* **101**, 048101.

KUMAR, D., RICHTER, C.M. & SCHROEDER, C.M. 2020 Conformational dynamics and phase behavior of lipid vesicles in a precisely controlled extensional flow. *Soft Matt.* **16**, 337–347.

LARSON, R.G. 1988 *Constitutive Equations for Polymer Melts and Solutions*. Butterworth-Heinemann.

LEE, J.S., DYLLA-SPEARS, R., TECLEMARIAM, N.P. & MULLER, S.J. 2007 Microfluidic four-roll mill for all flow types. *Appl. Phys. Lett.* **90** (7), 074103.

LUMLEY, J.L. 1969 Drag reduction by additives. *Annu. Rev. Fluid. Mech.* **1** (1), 367–384.

MENASVETA, M.J. & HOAGLAND, D.A. 1991 Light scattering from dilute poly(styrene) solutions in uniaxial elongational flow. *Macromolecules* **24** (11), 3427–3433.

NARSIMHAN, V., SPANN, A.P. & SHAQFEH, E.S.G. 2015 Pearling, wrinkling, and buckling of vesicles in elongational flows. *J. Fluid Mech.* **777**, 1–26.

OGDEN, R.W. 1984 *Nonlinear Elastic Deformations*. Dover.

PERKINS, T.T., SMITH, D.E. & CHU, S. 1997 Single polymer dynamics in an elongational flow. *Science* **276** (5321), 2016–2021.

PETERLIN, A. 1961 Streaming birefringence of soft linear macromolecules with finite chain length. *Polymer* **2**, 257–264.

PONTE CASTAÑEDA, P. 2005 *Heterogeneous Materials*. Lecture Notes, Department of Mechanics. Ecole Polytechnique.

ROSCOE, R. 1967 On the rheology of a suspension of viscoelastic spheres in a viscous liquid. *J. Fluid Mech.* **28**, 273–293.

SCHROEDER, C.M., SHAQFEH, E.S.G. & CHU, S. 2004 Effect of hydrodynamic interactions on DNA dynamics in extensional flow: simulation and single molecule experiment. *Macromolecules* **37** (24), 9242–9256.

SCHROEDER, C.M., TEIXEIRA, R.E., SHAQFEH, E.S.G. & CHU, S. 2005 Characteristic periodic motion of polymers in shear flow. *Phys. Rev. Lett.* **95**, 018301.

SILMORE, K.S., STRANO, M.S. & SWAN, J.W. 2021 Buckling, crumpling, and tumbling of semiflexible sheets in simple shear flow. *Soft Matt.* **17**, 4707–4718.

SMITH, D.E., BABCOCK, H.P. & CHU, S. 1999 Single-polymer dynamics in steady shear flow. *Science* **283** (5408), 1724–1727.

SMITH, D.E. & CHU, S. 1998 Response of flexible polymers to a sudden elongational flow. *Science* **281** (5381), 1335–1340.

TANNER, R.I. 1975 Stresses in dilute solutions of bead-nonlinear-spring macromolecules. III. Friction coefficient varying with dumbbell extension. *Trans. Soc. Rheol.* **19** (4), 557–582.

TEIXEIRA, R.E., BABCOCK, H.P., SHAQFEH, E.S.G. & CHU, S. 2005 Shear thinning and tumbling dynamics of single polymers in the flow-gradient plane. *Macromolecules* **38** (2), 581–592.

WETZEL, E.D. & TUCKER, C.L. 2001 Droplet deformation in dispersions with unequal viscosities and zero interfacial tension. *J. Fluid Mech.* **426**, 199–228.

WILLIS, J.R. 1981 Variational and related methods for the overall properties of composites. *Adv. Appl. Mech.* **21**, 1–78.

YEOH, O.H. 1993 Some forms of the strain energy function for rubber. *Rubber Chem. Technol.* **66**, 754–771.

YU, Y. & GRAHAM, M.D. 2021 Coil-stretch-like transition of elastic sheets in extensional flows. *Soft Matt.* **17**, 543–553.

YU, Y. & GRAHAM, M.D. 2022 Wrinkling and multiplicity in the dynamics of deformable sheets in uniaxial extensional flow. *Phys. Rev. Fluids* **7**, 023601.